# Recent applications of the Tübingen-Vienna Smooth Particle Hydrodynamics code

Christoph M. Schäfer* , Thomas I. Maindl†, Christoph Burger†, and Oliver J. Wandel*
* Institute for Astronomy and Astrophysics, Eberhard-Karls-Universität Tübingen, Tübingen, Germany
{ch.schaefer,oliver.wandel}@uni-tuebingen.de
† Department of Astrophysics, University of Vienna, Vienna, Austria
{thomas.maindl,c.burger}@univie.ac.at

***Abstract*—Here, we present the latest improvements and applications of the Tübingen-Vienna Smooth Particle Hydrodynamics (SPH) code. By the use of modern graphics processing units (GPUs), we have increased the performance of astrophysical simulations in the field of hydrodynamics and solid mechanics by porting an OpenMP code to the GPU with CUDA™. Recently, we have added a porosity module and a soil module to our existing framework. The code is freely available upon request.**

***Index Terms*—smooth particle hydrodynamics, modelling, computational astrophysics**

## I. Introduction

SPH was firstly introduced as a grid-free Lagrangian particle method for solving the system of hydrodynamic equations for compressible and viscous fluids by [7] and [13]. SPH is especially suited for boundary-free problems with high density contrasts. Rather than being solved on a grid, the equations are solved at the positions of the so-called particles, each of which represents a volume of the fluid with its physical quantities like mass, density, temperature, etc. and moves with the flow according to the equations of motion. The method was extended to solid mechanics in the beginning of the nineties by [10] and improved extensively in the following years [11], [12], [14]. The extension to model granular media and soil has been successfully added to SPH in the last years [2].

A recent development in high performance computing is to harness the power of GPUs for massive parallel applications. The most advanced interface for general purpose GPU programming is CUDA from Nvidia. We have successfully used the CUDA framework to accelerate our existing SPH code [16] and present here new modules that have been added to the framework lately. In the subsequent section, we will describe the physical models and equations and the numerical scheme to solve them. We will present three recent applications of our numerical framework in its subsequent section. Eventually, we will conclude in the last section.

## II. Physical and Numerical Models

### A. Basic equations

The system of partial differential equations that describe the dynamics of an elastic solid body is given by the three equations for the conservation of mass, momentum and (internal) energy, respectively. The conservation of mass is given by the continuity equation, which reads

$$\frac{\mathrm{d}\varrho}{\mathrm{d}t} + \varrho \frac{\partial v^\alpha}{\partial x^\alpha} = 0, \tag{1}$$

where $\varrho$ denotes the density and $\mathbf{v}$ the velocity and the Einstein summation rule is applied. Greek indices denote the spatial coordinates and run from 1 to 3. The second equation in the system accounts for the conservation of momentum

$$\frac{\mathrm{d}v^\alpha}{\mathrm{d}t} = \frac{1}{\varrho}\frac{\partial \sigma^{\alpha\beta}}{\partial x^\beta}. \tag{2}$$

The stress tensor $\sigma$ is given by the pressure $p$ and the deviatoric stress tensor $S^{\alpha\beta}$

$$\sigma^{\alpha\beta} = -p\delta^{\alpha\beta} + S^{\alpha\beta}. \tag{3}$$

In contrast to fluid dynamics, this set of partial differential conservation equations is not sufficient to describe the elastic body. Additionally the time evolution of the deviatoric stress tensor has to be specified. The missing relations are called the constitutive equations which describe the rheology of the body and relate the kinematic states of the body to the dynamic states. The time evolution of the deviatoric stress tensor can be expressed as

$$\frac{\mathrm{d}S^{\alpha\beta}}{\mathrm{d}t} = 2\mu\left[\dot{\varepsilon}^{\alpha\beta} - \frac{1}{3}\delta^{\alpha\beta}\dot{\varepsilon}^{\gamma\gamma}\right] + S^{\alpha\gamma}R^{\gamma\beta} + S^{\beta\gamma}R^{\gamma\alpha}, \tag{4}$$

where $R^{\alpha\beta}$ denotes the rotation rate tensor

$$R^{\alpha\beta} = \frac{1}{2}\left(\frac{\partial v^\alpha}{\partial x^\beta} - \frac{\partial v^\beta}{\partial x^\alpha}\right), \tag{5}$$

and $\dot{\varepsilon}^{\alpha\beta}$ the strain rate tensor

$$\dot{\varepsilon}^{\alpha\beta} = \frac{1}{2}\left(\frac{\partial v^\alpha}{\partial x^\beta} + \frac{\partial v^\beta}{\partial x^\alpha}\right). \tag{6}$$

The closure of this set of partial differential equations is given by the equation of state (eos). The eos relates the thermodynamic variables density $\varrho$, pressure $p$, and specific internal energy $u$. Currently, our framework allows to choose between several eos, which are described in more detail in the following.

### B. Equation of State

*1) Murnaghan eos:* The Murnaghan eos is often used to model the behaviour of solids under high pressure conditions. The pressure depends non-linearly on the density

$$p = \frac{K_0}{n}\left[\left(\frac{\varrho}{\varrho_0}\right)^n - 1\right], \tag{7}$$

with the zero pressure bulk modulus $K_0$ and the constant $n$. The Murnaghan eos is limited to isothermal compression.

*2) Tillotson eos:* The Tillotson eos distinguishes between two different domains depending on the specific internal energy $u$. In the case of compressed regions ($\varrho \geq \varrho_0$) and $u$ lower than the energy of incipient vaporization $e_{\text{iv}}$ pressure is given by

$$p = \left[a + \frac{b}{1 + u/(e_0\eta^2)}\right]\varrho u + A\xi + B\xi^2, \tag{8}$$

with $\eta = \varrho/\varrho_0$ and $\xi = \eta - 1$. In case of expanded material ($u$ greater than the energy of complete vaporization $e_{\text{cv}}$) the eos takes the form

$$\begin{aligned} p =& a\varrho u + \left[\frac{b\varrho u}{1 + u/(e_0\eta^2)}\right. \\ &\left. + A\xi \exp\left\{-\beta\left(\frac{\varrho_0}{\varrho} - 1\right)\right\}\right] \\ &\times \exp\left\{-\alpha\left(\frac{\varrho_0}{\varrho} - 1\right)^2\right\}. \end{aligned} \tag{9}$$

The symbols $\varrho_0$, $A$, $B$, $e_0$, $a$, $b$, $\alpha$, and $\beta$ are material dependent parameters. In the partial vaporization regime $e_{\text{iv}} < u < e_{\text{cv}}$, the pressure is linearly interpolated between the pressures obtained via (8) and (9), respectively.

*3) Ideal gas eos:* For the simulation of gases, the framework includes the ideal gas equation

$$p = \left(\frac{c_p}{c_V} - 1\right)\varrho u, \tag{10}$$

where $c_p$ and $c_V$ denote the specific heat capacities at constant pressure and volume, respectively.

### C. Porosity model

In order to model subresolution porosity, we have implemented the $p$-$\alpha$ model. The basic idea of this porosity model is the separation of the volume change in a porous material into the collapse of the pores and the compression of the matrix material. The distention is a measure for the porosity of the material and defined as follows

$$\alpha = \frac{\varrho_s}{\varrho}, \tag{11}$$

where $\varrho$ is the density of the porous material and $\varrho_s$ the density of the corresponding matrix material. The pressure of the porous material is then determined by the experimentally found relation between the pressure $p_s$ of the solid material and the porosity or distention [6]

$$p = \frac{1}{\alpha}p_s(\varrho_s, u_s) = \frac{1}{\alpha}p_s(\alpha\varrho, u). \tag{12}$$

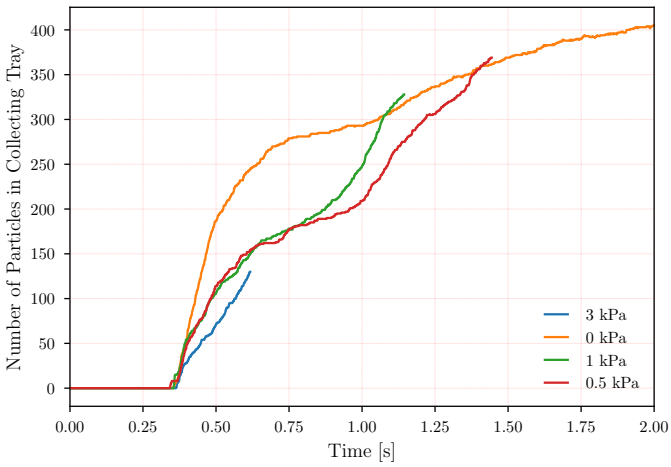


Figure 1. Sampling process on Phobos' surface for different material properties of regolith: The angle of internal friction is $\phi = 42\,\text{deg}$ and the cohesion $c$ varies with 0 Pa, 500 Pa, 1000 Pa and 3000 Pa.

Here, $u_s$ denotes the specific internal energy of the solid matrix material. In addition to the basic conservation equations, the evolution of the distention is also integrated to determine the change of porosity during compaction [18].

### D. Rheology model for regolith

The plastic flow of regolith can be modelled by the Drucker-Prager yield criterion. In the Drucker-Prager model, the yield function $f$ is given by the relation between the first and second invariant of the stress tensor

$$f(I_1, J_2) = \sqrt{J_2} + \alpha_\phi I_1 - k_c = 0. \tag{13}$$

The invariants are given by the following terms

$$I_1 = \text{tr}(\sigma) = \sigma^{\gamma\gamma} \quad \text{and} \quad J_2 = \frac{1}{2}S^{\alpha\beta}S_{\alpha\beta}. \tag{14}$$

The two material constants $\alpha_\phi$ and $k_c$ are called Drucker-Prager constants and are related to the material constants cohesion $c$ and angle of internal friction $\phi$ in the following way (for plane strain conditions)

$$\alpha_\phi = \frac{\tan\phi}{\sqrt{9 + 12\tan^2\phi}} \quad \text{and} \quad k_c = \frac{3c}{\sqrt{9 + 12\tan^2\phi}}. \tag{15}$$

### E. Self-gravity

The code implements a Barnes-Hut tree that allows for treatment of self-gravity. We follow the efficient implementation by [5].

## III. Applications

In this section, we summarize three recently presented applications of the computational framework: modelling a possible sampling process on Phobos, collisions between planetary embryos and impacts of smaller objects into asteroids.

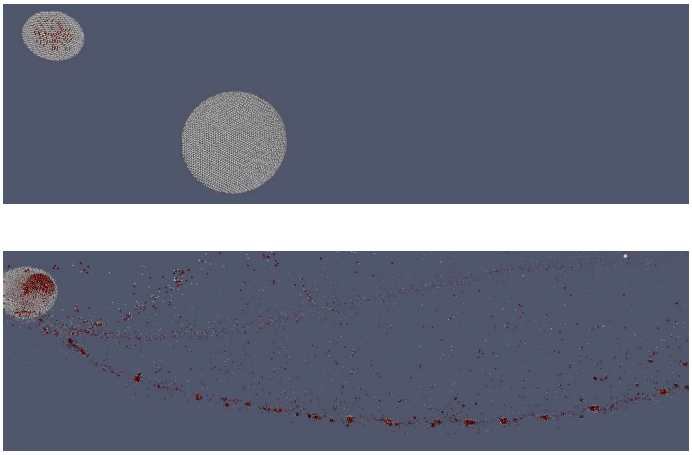

Figure 2. Chain forming simulation of two planetary embryos. The total mass of the system is $10^{23}$ kg and the mass ratio between projectile and target object is 1:9. The impact angle of this simulation is 30 deg and the impact speed was 2.5 $\times$ the mutual escape velocity. The upper panel shows the initial setup of the collision and the lower panel the formed chain.

### A. Sampling on Phobos

The surface of the Mars moon Phobos is covered with regolith and the thickness of the layer varies between 5 m and 100 m. The European Space Agency (ESA) currently investigates the implementation of a sample return mission to Phobos. We developed a SPH model for one specific sampling tool design and performed several simulations with different conditions regarding the material properties of the regolith. Our implementation is based on the model developed by [2], a model for granular flow using SPH in the context of solid mechanics combined with a Drucker-Prager yield criterion for plastic flow. The sampling speed for different material properties of regolith is shown in figure 1. A detailed description of the project and the results of more simulations can be found in [17].

### B. Collisions between planetary embryos

The Tübingen-Vienna SPH code has been successfully applied to the simulation of collisions between planetary embryos. Each of the two colliding planetary embryos consists of an iron core with a basaltic mantle and an outer ice shell as described in [3] and [4]. We trace the fate of the ice and water in these collisions. The outcome of a special chain-forming collision is shown in Figure 2.

### C. Impacts of smaller objects into asteroids

Active asteroids are objects in the asteroid belt that are dynamically similar to asteroids, but show activity and mass loss like comets. The mass loss is triggered by impacts of meter-sized objects in these asteroids that can form craters up to 12 m in diameter [8]. The crater shaped by such an impact is shown in Figure 3.

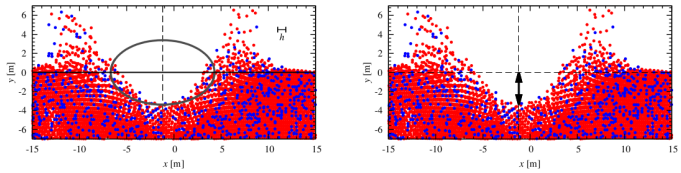


Figure 3. Impact crater formation on a Main-belt comet. Simulational outcome of a typical impact simulation. The diameter of the impactor was 1 m and the impact speed was 4.4 km s$^{-1}$ [8].

## IV. Conclusion

We presented three recent applications of the Tübingen-Vienna SPH code, where two of them featured our newly implemented porosity and regolith/soil modules. The bwForCluster BinAC is specially suited for our purposes since it enables us to cover a vast material parameter space with high resolution. Often, in our kind of simulations, the material data is scarce and many different properties of the material have to be varied and respected, leading to a high number of simulations. The code is freely available to the astrophysical and geophysical community upon request by email to the authors.

Our intention is to extend the existing code to multi GPUs support, which will allow for even higher resolutions. The demand for higher resolution is prevailing in the field of planet formation, since collisions between planetary cores indicate that the existing simulations do not show convergence yet [15].

## Acknowledgments

The authors acknowledge support by the High Performance and Cloud Computing Group at the Zentrum für Datenverarbeitung of the University of Tübingen, the state of Baden-Württemberg through bwHPC and the German Research Foundation (DFG) through grant no INST 37/935-1 FUGG. Some material is based on the work performed on behalf of the industrial Phobos Sample Return Phase A study team of Airbus Defense and Space under ESA contract 4000114302/15/NL/PA (technical officer: Thomas Voirin). CB and TIM appreciate support by the FWF Austrian Science Fund project S 11603-N16. CMS wants to thank Daniel Thun for helpful discussions during the course of these projects. The plots in this publication have been made by the use of the matplotlib package by [9] and paraview [1].

## References

[1] U. Ayachit, *The ParaView Guide: A Parallel Visualization Application*, 2015.

[2] H. H. Bui, R. Fukagawa, K. Sako, and S. Ohno, "Lagrangian meshfree particles method (sph) for large deformation and failure flows of geomaterial using elastic–plastic soil constitutive model," *International Journal for Numerical and Analytical Methods in Geomechanics*, vol. 32, no. 12, pp. 1537–1570, 2008.

[3] C. Burger and C. M. Schäfer, "Applicability and limits of simple hydrodynamic scaling for collisions of water-rich bodies in different mass regimes," *Proceedings of the First Greek-Austrian Workshop on Extrasolar Planetary Systems*, pp. 63–81, Mar. 2017.

[4] C. Burger and C. M. Schäfer, "Water transfer and loss in hit-and-run collisions," *accepted for publication in Celestial Mechanics and Dynamical Astronomy*, 2017.
[5] M. Burtscher, *GPU Computing Gems Emerald Edition*, W. Hwu, Ed., 2011.
[6] M. M. Carroll and A. C. Holt, "Static and dynamic pore-collapse relations for ductile porous materials," *Journal of Applied Physics*, vol. 43, no. 4, pp. 1626–1636, 1972. [Online]. Available: https://doi.org/10.1063/1.1661372
[7] R. A. Gingold and J. J. Monaghan, "Smoothed particle hydrodynamics: Theory and application to non-spherical stars," *MNRAS*, vol. 181, pp. 375–389, 1977.
[8] N. Haghighipour, T. I. Maindl, C. Schäfer, R. Speith, and R. Dvorak, "Triggering Sublimation-driven Activity of Main Belt Comets," *ApJ*, vol. 830, p. 22, Oct. 2016.
[9] J. D. Hunter, "Matplotlib: A 2d graphics environment," *Computing In Science & Engineering*, vol. 9, no. 3, pp. 90–95, 2007.
[10] L. D. Libersky and A. G. Petschek, *Smooth Particle Hydrodynamics with Strength of Materials*. Springer Verlag, 1990, p. 248.
[11] L. D. Libersky, A. G. Petschek, T. C. Carney, J. R. Hipp, and F. A. Allahdadi, "High strain lagrangian hydrodynamics," *J. Chem. Phys.*, vol. 109, p. 67, 1993.
[12] L. D. Libersky, P. W. Randles, T. C. Carney, and D. L. Dickinson, "Recent improvements in sph modeling of hypervelocity impact," *Int. J. Impact Eng.*, vol. 20, p. 525, 1997.
[13] L. B. Lucy, "A numerical approach to the testing of the fission hypothesis," *AJ*, vol. 82, no. 12, pp. 1013–1024, 1977.
[14] P. W. Randles and L. D. Libersky, "Smoothed Particle Hydrodynamics: Some recent improvements and applications," *Comp. Methods Appl. Mech. Engrg.*, vol. 139, p. 375, 1996.
[15] C. Reinhardt and J. Stadel, "Numerical aspects of giant impact simulations," *MNRAS*, vol. 467, pp. 4252–4263, Jun. 2017.
[16] C. Schäfer, S. Riecker, T. I. Maindl, R. Speith, S. Scherrer, and W. Kley, "A smooth particle hydrodynamics code to model collisions between solid, self-gravitating objects," *A&A*, vol. 590, p. A19, May 2016.
[17] C. M. Schäfer, S. Scherrer, R. Buchwald, T. I. Maindl, R. Speith, and W. Kley, "Numerical simulations of regolith sampling processes," *Planet. Space Sci.*, vol. 141, pp. 35–44, Jul. 2017.
[18] O. J. Wandel, C. M. Schäfer, and T. I. Maindl, "Collisional fragmentation of porous objects in planetary systems," *Proceedings of the First Greek-Austrian Workshop on Extrasolar Planetary Systems*, pp. 225–242, Mar. 2017.